

- Timmons, L., Court, D. L. & Fire, A. Ingestion of bacterially expressed dsRNAs can produce specific and potent genetic interference in *Caenorhabditis elegans*. *Gene* **263**, 103–112 (2001).
- Tavernarakis, N., Wang, S. L., Dorovkov, M., Ryazanov, A. & Driscoll, M. Heritable and inducible genetic interference by double-stranded RNA encoded by transgenes. *Nature Genet.* **24**, 180–183 (2000).
- McIntire, S. L., Reimer, R. J., Schuske, K., Edwards, R. H. & Jorgensen, E. M. Identification and characterization of the vesicular GABA transporter. *Nature* **389**, 870–876 (1997).
- Beitel, G. J., Tuck, S., Greenwald, I. & Horvitz, H. R. The *Caenorhabditis elegans* gene *lin-1* encodes an ETS-domain protein and defines a branch of the vulval induction pathway. *Genes Dev.* **9**, 3149–3162 (1995).
- Zuo, Y. & Deutscher, M. P. Exoribonuclease superfamilies: structural analysis and phylogenetic distribution. *Nucleic Acids Res.* **29**, 1017–1026 (2001).
- Li, Z., Pandit, S. & Deutscher, M. P. 3' exoribonucleolytic trimming is a common feature of the maturation of small, stable RNAs in *Escherichia coli*. *Proc. Natl Acad. Sci. USA* **95**, 2856–2861 (1998).
- Ghosh, S. & Deutscher, M. P. Oligoribonuclease is an essential component of the mRNA decay pathway. *Proc. Natl Acad. Sci. USA* **96**, 4372–4377 (1999).
- Dominski, Z., Yang, X. C., Kaygun, H., Dadlez, M. & Marzluff, W. F. A 3' exonuclease that specifically interacts with the 3' end of histone mRNA. *Mol. Cell* **12**, 295–305 (2003).
- Kipp, M. *et al.* SAF-box, a conserved protein domain that specifically recognizes scaffold attachment region DNA. *Mol. Cell Biol.* **20**, 7480–7489 (2000).
- Hamdan, S., Carr, P. D., Brown, S. E., Ollis, D. L. & Dixon, N. E. Structural basis for proofreading during replication of the *Escherichia coli* chromosome. *Structure Fold. Des.* **10**, 535–546 (2002).
- Zamore, P. D., Tuschl, T., Sharp, P. A. & Bartel, D. P. RNAi: double-stranded RNA directs the ATP-dependent cleavage of mRNA at 21 to 23 nucleotide intervals. *Cell* **101**, 25–33 (2000).
- Elbashir, S. M., Martinez, J., Patkaniowska, A., Lendeckel, W. & Tuschl, T. Functional anatomy of siRNAs for mediating efficient RNAi in *Drosophila melanogaster* embryo lysate. *EMBO J.* **20**, 6877–6888 (2001).
- Caplen, N. J., Parrish, S., Imani, F., Fire, A. & Morgan, R. A. Specific inhibition of gene expression by small double-stranded RNAs in invertebrate and vertebrate systems. *Proc. Natl Acad. Sci. USA* **98**, 9742–9747 (2001).
- Simmer, F. *et al.* Loss of the putative RNA-directed RNA polymerase RRF-3 makes *C. elegans* hypersensitive to RNAi. *Curr. Biol.* **12**, 1317–1319 (2002).
- Tabara, H. *et al.* The *rde-1* gene, RNA interference, and transposon silencing in *C. elegans*. *Cell* **99**, 123–132 (1999).
- Tabara, H., Yigit, E., Siomi, H. & Mello, C. C. The dsRNA binding protein RDE-4 interacts with RDE-1, DCR-1, and a DExH-box helicase to direct RNAi in *C. elegans*. *Cell* **109**, 861–871 (2002).
- Winston, W. M., Molodowitch, C. & Hunter, C. P. Systemic RNAi in *C. elegans* requires the putative transmembrane protein SID-1. *Science* **295**, 2456–2459 (2002).
- Sijen, T. *et al.* On the role of RNA amplification in dsRNA-triggered gene silencing. *Cell* **107**, 465–476 (2001).
- Gu, T., Orita, S. & Han, M. *Caenorhabditis elegans* SUR-5, a novel but conserved protein, negatively regulates LET-60 Ras activity during vulval induction. *Mol. Cell Biol.* **18**, 4556–4564 (1998).

Supplementary Information accompanies the paper on [www.nature.com/nature](http://www.nature.com/nature).

**Acknowledgements** We thank J. Roig, G. Lenz and J. Avruch for reagents and advice; A. Frand for critically evaluating our manuscript; and members of the Ruvkun laboratory for advice and discussions.

**Competing interests statement** The authors declare that they have no competing financial interests.

**Correspondence** and requests for materials should be addressed to G.R. ([ruvkun@molbio.mgh.harvard.edu](mailto:ruvkun@molbio.mgh.harvard.edu)).

## Cytoplasmic dynein functions as a gear in response to load

Roop Mallik<sup>1</sup>, Brian C. Carter<sup>1</sup>, Stephanie A. Lex<sup>2</sup>, Stephen J. King<sup>2</sup> & Steven P. Gross<sup>1</sup>

<sup>1</sup>Department of Developmental and Cell Biology, University of California Irvine, Irvine, California 92612, USA

<sup>2</sup>Division of Molecular Biology and Biochemistry, School of Biological Sciences, University of Missouri-Kansas City, Kansas City, Missouri 64110, USA

Cytoskeletal molecular motors belonging to the kinesin and dynein families transport cargos (for example, messenger RNA, endosomes, virus) on polymerized linear structures called microtubules in the cell<sup>1</sup>. These 'nanomachines' use energy obtained from ATP hydrolysis to generate force<sup>2</sup>, and move in a step-like manner on microtubules. Dynein<sup>3–5</sup> has a complex and funda-

mentally different structure from other motor families. Thus, understanding dynein's force generation can yield new insight into the architecture and function of nanomachines. Here, we use an optical trap<sup>6</sup> to quantify motion of polystyrene beads driven along microtubules by single cytoplasmic dynein motors. Under no load, dynein moves predominantly with a mixture of 24-nm and 32-nm steps. When moving against load applied by an optical trap, dynein can decrease step size to 8 nm and produce force up to 1.1 pN. This correlation between step size and force production is consistent with a molecular gear mechanism. The ability to take smaller but more powerful strokes under load—that is, to shift gears—depends on the availability of ATP. We propose a model whereby the gear is downshifted through load-induced binding of ATP at secondary sites in the dynein head.

Cytoplasmic dynein is responsible for most intracellular retrograde (towards microtubule minus ends) transport as well as chromosome segregation during mitosis<sup>4,5</sup>. To understand its function in a controlled setting, purified cytoplasmic dynein was adsorbed on beads that served as markers for motor position<sup>7</sup> (see Methods). An optical trap was used to place dynein-coated beads on immobilized microtubules. The microtubule-binding probability of beads followed single-molecule Poisson statistics, suggesting that processive motion was driven by single dynein molecules<sup>8</sup> (Fig. 1a; see also Supplementary Fig. 2). Motor function was quantified using video tracking<sup>9</sup> and an optical trap with a quadrant photodiode detector<sup>10</sup> (see Methods). The force exerted by the motor was determined from the product of trap stiffness and displacement

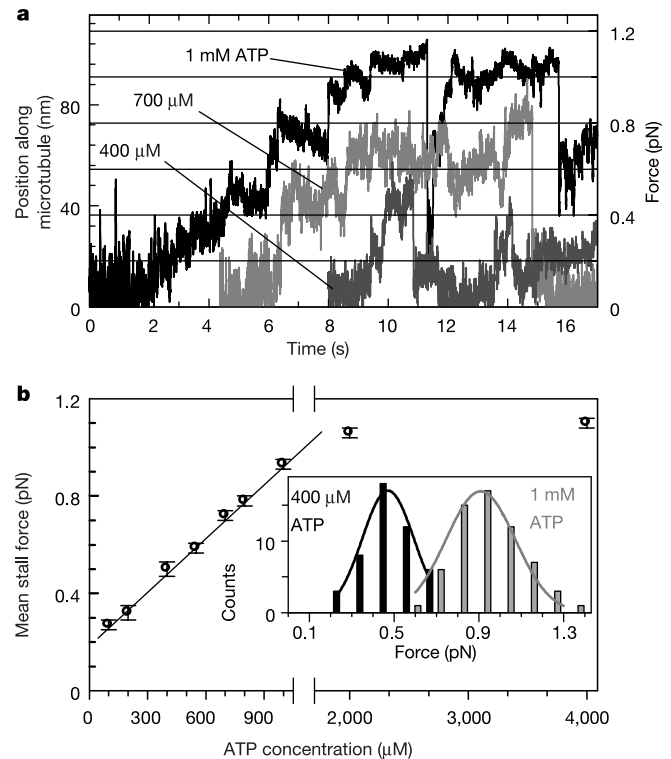


**Figure 1** Stall force of cytoplasmic dynein. **a**, Quadrant photodetector record of dynein-driven bead motion in the optical trap, at different ATP concentrations. Time axis origin is adjusted for clarity. **b**, Mean stall force ( $\pm$ s.e.m.) from multiple displacement records as a function of ATP. A straight line emphasizes linearity of the data below 1 mM ATP. Inset, distribution of stall force at 400  $\mu$ M and 1 mM ATP. Solid lines show gaussian fits to the respective data (400  $\mu$ M ATP, mean = 0.50 pN,  $\sigma$  = 0.26 pN,  $n$  = 47; 1 mM ATP, mean = 0.92 pN,  $\sigma$  = 0.31 pN,  $n$  = 62).

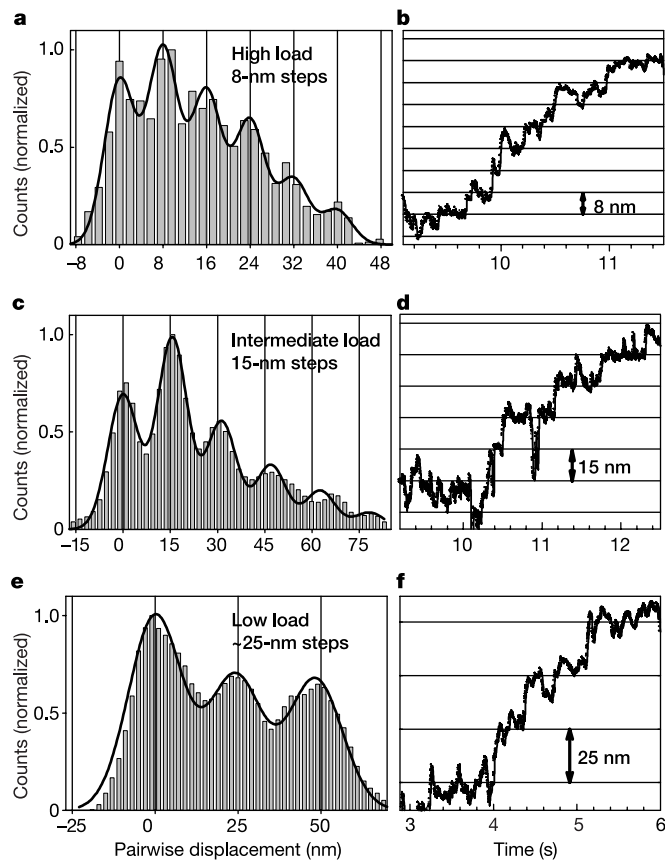


**Figure 2** Dynein takes shorter steps under load. **a**, Pairwise distance function (PDF) of displacements under load approaching stall ( $>0.8$  pN). The solid line is fitted to the sum of six gaussians,  $i = -2$  to  $3$ ,  $\sum_i A_i \exp[-(x - i\Delta)^2 / (2\sigma^2)]$ , where  $\Delta$  is the unit step size,  $A_i$  is the amplitude and  $\sigma$  is the standard deviation. After correction for bead-linkage stiffness (see Methods),  $\Delta = 7.9$  nm,  $\sigma = 2.8$  nm. **b**, Eight-nanometre steps in the displacement record. Data are median filtered with a 10-ms time window. Trap stiffness =  $0.011$  pN nm $^{-1}$ . **c**, PDF of displacements at intermediate load (about 0.40–0.80 pN). The solid line is fitted to the sum of six gaussians,  $\Delta = 15.5$  nm,  $\sigma = 4.8$  nm. **d**, Fifteen-nanometre steps. Trap stiffness =  $0.007$  pN nm $^{-1}$ . **e**, PDF of displacements at low load ( $<0.4$  pN). The solid line is fit to the sum of three gaussians,  $\Delta = 25.3$  nm,  $\sigma = 8.1$  nm. **f**, Twenty-five-nanometre steps. Trap stiffness =  $0.007$  pN nm $^{-1}$ . Each plot is a representative example of multiple recordings. In a given load range, a mixture of different step sizes cannot be ruled out.

of the bead from the trap centre, after correction for bead–microtubule linkage stiffness<sup>8</sup> (see Methods).

Plotted as a function of ATP concentration (Fig. 1b), the mean stall force increases linearly up to 1 mM ATP, beyond which it reaches a maximum value of 1.1 pN. At 100  $\mu$ M ATP the maximum force produced is only about 0.25 pN, a reduction of approximately 75% from the stall force value at saturating (4 mM) ATP. The magnitude of this reduction is much larger than for kinesin<sup>11</sup>. The distribution of stall forces at 400  $\mu$ M and 1 mM ATP (Fig. 1b, inset) demonstrates a population shift from ‘weaker’ to ‘stronger’ motor species as the ATP concentration increases. The maximal stall force of 1.1 pN at saturating ATP is similar to that observed for axonemal dynein from inner arm of *Chlamydomonas* flagella<sup>12</sup>, and is consistent with the predicted *in vivo* stall force of  $1.1 \pm 0.04$  pN for a single cytoplasmic dynein<sup>13</sup>.

To investigate further motor function at high ATP, the size of unitary steps of dynein was obtained from the pairwise distance function (PDF) of bead displacement records<sup>14</sup>. A representative

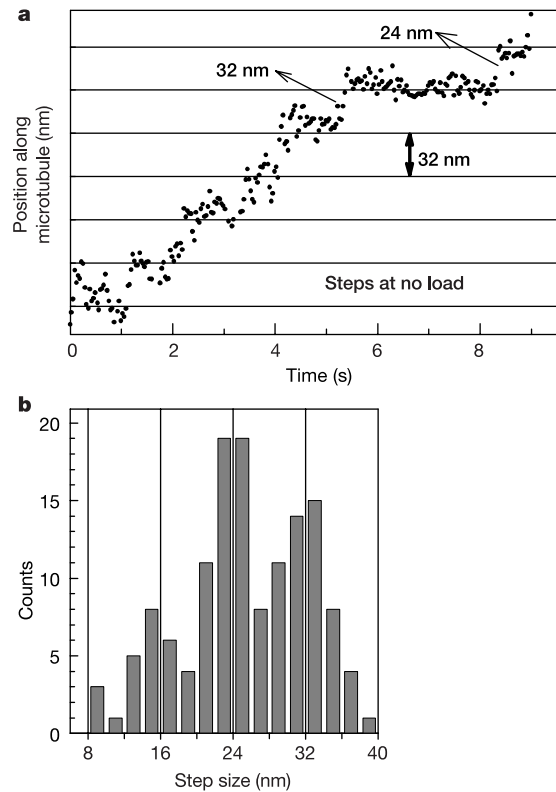


**Figure 3** Cytoplasmic dynein takes predominantly 24- and 32-nm steps under no load. **a**, Representative video track of bead driven by single dynein molecule at 2  $\mu$ M ATP. The displacement parallel to the microtubule axis is plotted. One 24-nm and another 32-nm step are marked. **b**, Histogram showing the distribution of step sizes under no load. Vertical grids mark the microtubule lattice periodicity of 8 nm.

histogram of PDF plots from the high-load regime (load  $>0.8$  pN) shows a periodicity of 8 nm in the displacement record (Fig. 2a). Consecutive 8-nm steps in the raw displacement record are also shown (Fig. 2b). Thus, under high load cytoplasmic dynein takes steps of 8 nm. As dynein function might be regulated through variation in step size, we calculated the PDF for displacement under intermediate load conditions (about 0.4 to 0.8 pN). A periodicity of 15 nm was found (Fig. 2c, d). Such a step size was predicted for axonemal dynein from electron microscopic studies<sup>15</sup>. Under conditions approaching zero load ( $<0.4$  pN), we observed a periodicity of approximately 25 nm (Fig. 2e, f). Note that this is the same bead displacement record that yielded 15-nm steps at higher load (see above). Thus, the same motor steps in approximately 25-nm increments when under low load, and then reduces step size to 15 nm as it encounters increasing load moving away from the trap centre. Because of the large (about 25 nm) step size, only a limited number of steps occur in the optical trap before the increasing load presumably effects a transition to smaller steps. To investigate zero-load function further, we used video tracking<sup>9</sup> of unloaded beads (no optical trap). This tracking system was tested by moving dynein-bound beads with nanometre-sized, Poisson-distributed steps (see Supplementary Information).

At low (a few  $\mu$ M) ATP concentrations, ATP binding becomes rate limiting and individual motor steps can be detected with the temporal resolution of video tracking<sup>9,16</sup>. We observed a complex admixture of step sizes, with steps frequently close to 24 or 32 nm (Fig. 3a). The histogram of step sizes from multiple measurements (Fig. 3b; see also Supplementary Information) shows peaks at about

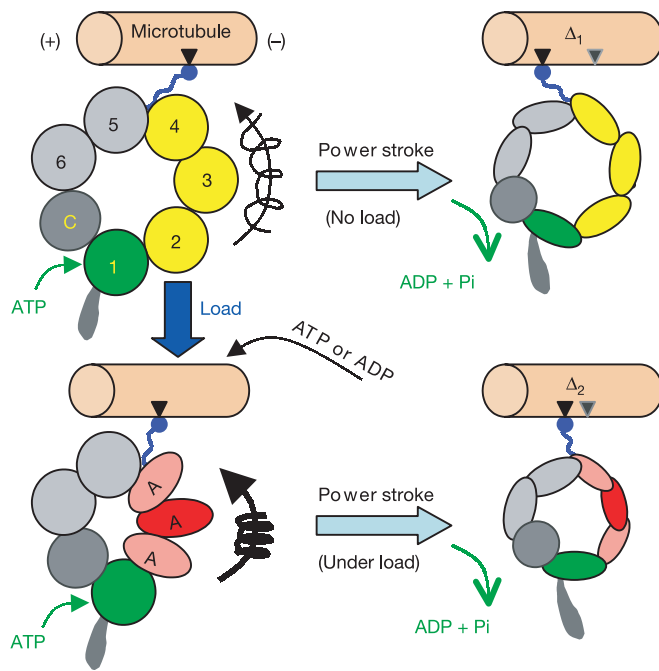


**Figure 4** Model for an ATP-regulated gear. The dynein head is shown as six sequential AAA domains (numbered spheres) and one carboxy-terminal subdomain (C) connected in a ring conformation with a projecting microtubule-binding stalk (blue). P<sub>i</sub>, phosphate group. Top panel: zero load. Primary ATP hydrolysis (at AAA number 1, green) causes propagating conformational change through domains 2–4 (yellow) leading to power stroke (left, before; right, after). The step size ( $\Delta_1$ ) is shown as distance between binding positions of the stalk on the microtubule (vertical arrowheads) before and after the power stroke. Bottom panel: function under load. Load-induced nucleotide (A indicates ATP or ADP) binding (at AAA number 3, dark red; possible also at numbers 2 and 4, light red) compacts ring conformation (note smaller diameter), resulting in a stiffer linkage (thick black arrow with spring) that can transmit higher force. The step size is now smaller ( $\Delta_2 < \Delta_1$ ).

15 nm, 24 nm and 32 nm. The combination of 24- and 32-nm steps might result from attempted steps of an intermediate magnitude (possibly 30 nm; see Supplementary Information) modulated by the microtubule lattice. Weak electrostatic interactions with the microtubule-binding sites could impose a backward (24-nm step) or forward (32-nm step) diffusive bias on the dynein head. Although only 8-nm steps are reported for axonemal dynein, published studies have characterized function only under high load<sup>12,17</sup>. Interestingly, axonemal dynein arms can produce oscillatory displacements<sup>18</sup> of a singlet microtubule with an amplitude of about 30 nm, which might reflect single back-and-forth steps with 30-nm magnitude close to the unloaded step size reported here (see Supplementary Information).

The distribution of residence times at low ATP shows a single-exponential decay (see Supplementary Information), and thus favours a 1:1 coupling scenario (single ATP hydrolysis gives single step) under no externally applied load<sup>19</sup>. With our data it is not possible to determine the coupling ratio at high load. However, the observed decrease in step size under load may indicate that the coupling remains unchanged, with the reduced step size resulting in a larger force—in other words, a gear mechanism. This is radically different from force production in kinesin<sup>14</sup> or myosin<sup>20</sup>, where step size under load is invariant. For a motor protein, the work done per step is:  $W_{\text{step}} = \text{step size} \times \text{stall force}$ . Using a step size of 32 nm and stall force of about 0.3 pN in the low-load regime,  $W_{\text{step}}$  is about 9.6 pN nm. At 4 mM ATP, with 8-nm step and 1.1-pN stall,  $W_{\text{step}}$  is about 8.8 pN nm. As  $W_{\text{step}}$  is almost unchanged (within experi-

mental error), the increase in stall force can be effected by the observed reduction in step size. Thus, from an energy conservation point of view there is no requirement of multiple ATP hydrolysis per step under load. About 90 pN nm of free energy is available from hydrolysis of a single ATP, so assuming 1:1 coupling, cytoplasmic dynein is roughly 10% efficient, in contrast to the approximately 50% efficiency of kinesin<sup>8</sup>.

How could such a nanoscale gear be implemented? Dynein is an AAA protein<sup>4,21,22</sup> (ATPase associated with diverse cellular activities), with complex architecture. It has four AAA domains (numbered 1 to 4), each of which can potentially bind ATP<sup>4,23</sup> (Fig. 4; see also Supplementary Information). It has been suggested<sup>22,24,25</sup> that nucleotide-binding-induced changes in relative orientation between adjacent AAA domains can lead to a ‘tighter’ conformation of the AAA ring (see Supplementary Information). Evidence for such ring compaction has been found in the NSF (*N*-ethylmaleimide-sensitive factor) AAA proteins<sup>26</sup>. We propose a dynein gear based on such a mechanism (Fig. 4), where load-induced ATP binding tightens the AAA ring, and yields a shorter but stronger step of the motor. In this extension of previous models<sup>3,22</sup>, ATP has the novel role of regulator of dynein step size, as well as being an energy input in the chemomechanical cycle. Could it be that dynein always generates a constant force of 1.1 pN, but under applied opposing load is unable to reach a distant binding site? Such a scenario does not agree with the stall force reduction at low ATP (Fig. 1b), where the motor is never observed to exert 1.1 pN force. The shortening of step size seems to arise out of a need to produce higher force, with the force-producing machinery (proposed gear mechanism) being disrupted by the unavailability of ATP. (See Supplementary Information for more information about the model.)

What are the implications of such a gear? Compared with the 8-nm steps in kinesin, at low load the 32-nm steps of dynein imply that as a cargo transporter, dynein is four times more fuel-efficient than kinesin. Furthermore, the ATP-dependent gear machinery of dynein is a potential target for dynein regulation. The single-molecule measurements presented here address a fundamental question in the field of molecular motors: why is the architecture of dynein so complex and different from that of kinesin or myosin? Our results suggest that this complexity implements a nanoscale transmission that enables dynein to shift gears, and minimize ATP consumption while providing force tailored to overcome external load. It will be an exciting challenge to apply the mechanical insights presented here to better understand other important AAA machines. □

## Methods

### Protein purification

Cytoplasmic dynein from bovine brain tissue was purified and isolated from dynactin as described<sup>27</sup>. Aliquots were flash frozen and stored at  $-80^\circ\text{C}$ . Before motility assay, dynein was further purified by an ATP-sensitive microtubule affinity assay<sup>28</sup>. Bovine brain tubulin was purified over a phosphocellulose column<sup>29</sup>. Absence of any significant contamination from dynactin was established through SDS-polyacrylamide gel electrophoresis (PAGE) gel (Supplementary Fig. 1).

### In vitro motility assay

Assays were performed at  $24^\circ\text{C}$  in a flow chamber ( $4 \times 25$  mm, volume approximately  $8 \mu\text{l}$ ) made with cleaned, polylysine-coated coverslips. Taxol-stabilized microtubules were immobilized on the coverslip surface before casein-blocking of surface. Dynein was first incubated with carboxylated polystyrene beads (450-nm diameter; Polysciences Inc.) in assay buffer (ATP plus  $0.3 \times 35$  mM PIPES, pH 7.2, 5 mM  $\text{MgSO}_4$ , 1 mM EGTA, 0.5 mM EDTA, plus 1 mM GTP plus  $20 \mu\text{M}$  Taxol). Further binding was blocked with casein ( $5 \text{ mg ml}^{-1}$  in assay buffer). Beads were viewed with video-enhanced differential interference contrast microscopy in an inverted microscope (modified Nikon TE-200). Custom-built image-processing software (Labview 6.1, National Instruments) was used for video tracking. Subpixel resolution in video tracking was confirmed as described<sup>15</sup>. Dynein-coated beads were brought into contact with microtubules using the optical trap. The fraction of beads binding to and moving on microtubules, when scored as a function of dynein:bead molar ratio, obeyed single-molecule Poisson statistics<sup>8,12,14,17,30</sup> (Supplementary Fig. 2). Assays were performed at a bead-to-microtubule binding fraction of 0.3 or less. At this concentration, taking into account geometric constraints applicable

to a random distribution<sup>8</sup> of dynein molecules on the bead, >99% of beads are driven by single dynein molecules.

Optical trapping was done as described<sup>6,10</sup> using an 830-nm single-mode diode laser (Melles Griot). Trap stiffness was calculated from the power spectrum of thermal fluctuations of trapped beads<sup>10</sup>. Back focal plane imaging of bead position in the optical trap was done with a quadrant photodiode detector<sup>10</sup>. The detector output was anti-alias filtered at 1 kHz and digitized at 2 kHz. The correction factor to the bead displacement<sup>8,12,17</sup> (about 1.06) due to elasticity of the bead–dynein linkage was determined from the variance of beads bound by motor to the microtubule in the presence of ADP, and from the trap stiffness.

Received 8 September; accepted 11 December 2003; doi:10.1038/nature02293.

- Hirokawa, N. Kinesin and dynein superfamily proteins and the mechanism of organelle transport. *Science* **279**, 519–526 (1998).
- Hackney, D. D. The kinetic cycles of myosin, kinesin and dynein. *Annu. Rev. Physiol.* **58**, 731–750 (1996).
- Asai, D. J. & Koonce, M. P. The dynein heavy chain: structure, mechanics and evolution. *Trends Cell Biol.* **11**, 196–202 (2001).
- King, S. M. AAA domains and organization of the dynein motor unit. *J. Cell Sci.* **113**, 2521–2526 (2000).
- King, S. M. The dynein microtubule motor. *Biochim. Biophys. Acta* **1496**, 60–75 (2000).
- Rice, S. E. & Spudich, J. A. Building and using optical traps to study properties of molecular motors. *Methods Enzymol.* **361**, 112–133 (2003).
- Wang, Z., Khan, S. & Sheetz, M. P. Single cytoplasmic dynein molecule movements: characterization and comparison with kinesin. *Biophys. J.* **69**, 2011–2023 (1995).
- Svoboda, K. & Block, S. M. Force and velocity measured for single kinesin molecules. *Cell* **77**, 773–784 (1994).
- Gelles, J., Schnapp, B. J. & Sheetz, M. P. Tracking kinesin-driven movements with nanometre-scale precision. *Nature* **331**, 450–453 (1988).
- Visscher, K. & Block, S. M. Versatile optical traps with feedback control. *Methods Enzymol.* **298**, 460–489 (1998).
- Visscher, K., Schnitzer, M. J. & Block, S. M. Single kinesin molecules studied with a molecular force clamp. *Nature* **400**, 184–189 (1999).
- Sakakibara, H., Kojima, H., Sakai, Y., Katayama, E. & Oiwa, K. Inner-arm dynein c of *Chlamydomonas* flagella is a single-headed processive motor. *Nature* **400**, 586–590 (1999).
- Gross, S. P., Welte, M. A., Block, S. M. & Wieschaus, E. F. Dynein-mediated cargo transport *in vivo*: A switch controls travel distance. *J. Cell Biol.* **148**, 945–955 (2000).
- Svoboda, K., Schmidt, C. F., Schnapp, B. J. & Block, S. M. Direct observation of kinesin stepping by optical trapping interferometry. *Nature* **365**, 721–727 (1993).
- Burgess, S. A., Walker, M. L., Sakakibara, H., Knight, P. J. & Oiwa, K. Dynein structure and power stroke. *Nature* **421**, 715–718 (2003).
- Hua, W., Young, E. C., Fleming, M. L. & Gelles, J. Coupling of kinesin steps to ATP hydrolysis. *Nature* **388**, 390–393 (1997).
- Hirakawa, E., Higuchi, H. & Toyoshima, Y. Y. Processive movement of single 22S dynein molecules occurs only at low ATP concentrations. *Proc. Natl Acad. Sci. USA* **97**, 2533–2537 (2000).
- Shingyoji, C., Higuchi, H., Yoshimura, M., Katayama, E. & Yanagida, T. Dynein arms are oscillating force generators. *Nature* **393**, 711–714 (1998).
- Schnitzer, M. J. & Block, S. M. Kinesin hydrolyses one ATP per 8-nm step. *Nature* **388**, 386–390 (1997).
- Mehta, A. D. *et al.* Myosin-V is a processive actin-based motor. *Nature* **400**, 590–593 (1999).
- Neuwald, A. F., Aravind, L., Spouge, J. L. & Koonin, E. V. AAA<sup>+</sup>: a class of chaperone-like ATPases associated with the assembly, operation and disassembly of protein complexes. *Genome Res.* **9**, 27–43 (1999).
- Vale, R. D. AAA proteins. Lords of the ring. *J. Cell Biol.* **150**, F13–F19 (2000).
- Samsó, M., Radermacher, M., Frank, J. & Koonce, M. P. Structural characterization of a dynein motor domain. *J. Mol. Biol.* **276**, 927–937 (1998).
- Silvanovich, A., Li, M., Serr, M., Mische, S. & Hays, T. S. The third P-loop domain in cytoplasmic dynein heavy chain is essential for dynein motor function and ATP-sensitive microtubule binding. *Mol. Biol. Cell* **14**, 1355–1365 (2003).
- Mocz, G. & Gibbons, I. R. Model for the motor component of dynein heavy chain based on homology to the AAA family of oligomeric ATPases. *Structure* **9**, 93–103 (2001).
- Whiteheart, S. W. *et al.* N-ethylmaleimide-sensitive fusion protein: a trimeric ATPase whose hydrolysis of ATP is required for membrane fusion. *J. Cell Biol.* **126**, 945–954 (1994).
- Bingham, J. B., King, S. J. & Schroer, T. A. Purification of dynactin and dynein from brain tissue. *Methods Enzymol.* **298**, 171–184 (1998).
- Schroer, T. A. & Sheetz, M. P. Two activators of microtubule-based vesicle transport. *J. Cell Biol.* **115**, 1309–1318 (1991).
- Sloboda, R. D. & Rosenbaum, J. L. Purification and assay of microtubule-associated proteins (MAPs). *Methods Enzymol.* **85**, 171–184 (1982).
- King, S. J. & Schroer, T. A. Dynactin increases the processivity of the cytoplasmic dynein motor. *Nature Cell Biol.* **2**, 20–24 (2000).

Supplementary Information accompanies the paper on [www.nature.com/nature](http://www.nature.com/nature).

**Acknowledgements** R.M. acknowledges a postdoctoral fellowship from the International Human Frontier Science Program Organization. B.C.C. acknowledges support from an NIH training grant. This work was supported by a NIGMS and a CRCC grant (to S.P.G.).

**Competing interests statement** The authors declare that they have no competing financial interests.

**Correspondence** and requests for materials should be addressed to S.P.G. (sgross@uci.edu).

## Structural basis for removal of adenine mispaired with 8-oxoguanine by MutY adenine DNA glycosylase

J. Christopher Fromme<sup>1</sup>, Anirban Banerjee<sup>2</sup>, Susan J. Huang<sup>1</sup> & Gregory L. Verdine<sup>1,2</sup>

<sup>1</sup>Department of Molecular and Cellular Biology, and <sup>2</sup>Department of Chemistry and Chemical Biology, Harvard University, Cambridge, Massachusetts 02138, USA

The genomes of aerobic organisms suffer chronic oxidation of guanine to the genotoxic product 8-oxoguanine (oxoG)<sup>1</sup>. Replicative DNA polymerases misread oxoG residues and insert adenine instead of cytosine opposite the oxidized base. Both bases in the resulting A•oxoG mismatch are mutagenic lesions, and both must undergo base-specific replacement to restore the original C•G pair. Doing so represents a formidable challenge to the DNA repair machinery, because adenine makes up roughly 25% of the bases in most genomes. The evolutionarily conserved enzyme adenine DNA glycosylase (called MutY in bacteria and hMYH in humans) initiates repair of A•oxoG to C•G by removing the inappropriately paired adenine base from the DNA backbone. A central issue concerning MutY function is the mechanism by which A•oxoG mismatches are targeted among the vast excess of A•T pairs. Here we report the use of disulphide crosslinking<sup>2</sup> to obtain high-resolution crystal structures of MutY–DNA lesion-recognition complexes. These structures reveal the basis for recognizing both lesions in the A•oxoG pair and for catalysing removal of the adenine base.

MutY (Fig. 1) belongs to a structural superfamily of proteins responsible for the base excision and repair of various genotoxic lesions. These proteins have a catalytic domain containing a

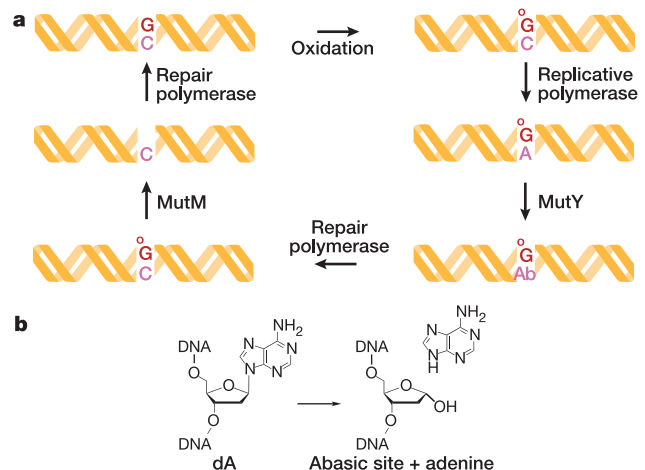


**Figure 1** Pathway for oxidation and repair of guanine in DNA. **a**, The initial oxidation product, oxoG•C, is misreplicated to produce oxoG•A. MutY removes the adenine nucleobase from oxoG•A pairs, generating an abasic site product (Ab refers to the product shown in **b**). Further processing by other enzymes results in restoration of the oxoG•C pair. Repair of oxoG•C by oxoG DNA glycosylase (MutM in bacteria, hOGG1 in eukaryotes) effects removal of the oxoG nucleoside, facilitating the final phase of repair, which generates the original G•C pair. **b**, Reaction catalysed by MutY.